



# Analysis of alkali-activated mineral wool-slag binders: evaluating the differences between one-part and two-part variations

Elijah Adesanya<sup>1</sup> · Rawia Dabbebi<sup>1</sup> · Christine Rößler<sup>2</sup> · Majda Pavlin<sup>3</sup> · Zhenming Li<sup>4</sup> · Tero Luukkonen<sup>1</sup> · Juho Yliniemi<sup>1</sup> · Mirja Illikainen<sup>1</sup>

Received: 14 August 2023 / Accepted: 11 December 2023 / Published online: 26 January 2024  
© The Author(s) 2024

## Abstract

Two synthesis pathways (one- and two-part) in alkali-activated binders were compared using ground granulated blast furnace slag (GGBFS), mineral wool (MW) activated using dry and liquid alkali activators with similar  $\text{Na}_2\text{O}/\text{SiO}_2$  modulus. The effect of activator type on reaction kinetics, strength development, setting times, and durability shows that one-part synthesis does not only improve early strength, but also provide better durability properties. While the highest compressive strength (56 MPa, 90 days) was achieved for the one-part mix (DM), the reaction products (presence of Mg–Al layered double hydroxide and C–S–H-like phases) observed for both mortar mixes were similar. The DM mortars showed better resistance to sulfate attack than two-part mix (WM) mortars and sets faster. The results highlight the significance of the one-part pathways in the synthesis of alkali-activated materials.

**Keywords** Blast furnace slag · Alkali activation · Glass wool · Stone wool · One-part · Two-part

## Introduction

Alkali-activated materials (AAMs), including geopolymers, have emerged as prominent Portland-cement-free alternative binders for concrete to curb the  $\text{CO}_2$  emissions of construction [1]. The main reaction products of AAMs consist of hydrous alkali and/or alkaline earth metal aluminosilicates forming either 3D network or interlinked chains as nanostructures when using low and high-calcium raw materials, respectively [2]. Interestingly, similar mineral phases have been identified in the binders of ~2000-year-old Roman concretes [3, 4], which gives a promising indication about the long-term durability of AAMs. Some critical factors to

achieve the full environmental benefits of AAMs include the selection of the alkali activator (especially avoiding synthetic alkali silicates) [5], considerations of transportation distances and locality of the raw materials [6], and, if aiming for a large-scale replacement of Portland cement, use of abundantly available natural minerals as raw materials instead of industrial side streams with frequently limited and fluctuating supply [7].

Alkali-activated materials can be prepared with two different approaches, which involve the use of alkali-activator solution or solid activator, and are referred in the literature commonly as two-part and one-part (or dry-mix) alkali activation, respectively [8]. Even though most of the current research and commercial applications focus on the two-part alkali activation, the early works published on AAMs employed solid activators [9, 10]. Nevertheless, the interest in the one-part AAMs has increased significantly in the last decade as indicated by the publication activity [8, 11] and recent patents on the topic [12, 13]. Using dry-form alkali activator, some practical issues related to the alkali-activator solutions are avoided, such as occupational hazards related to the handling of chemicals, high viscosity, tendency of sodium silicate to precipitate, and transportation of water in the solution [14]. On the other hand, the dry-form alkali activators (especially sodium hydroxide) may introduce some

✉ Elijah Adesanya  
elijah.adesanya@oulu.fi

<sup>1</sup> Faculty of Technology, Fiber and Particle Engineering Research Unit, University of Oulu, Oulu, Finland

<sup>2</sup> F.A. Finger-Institute for Building Material Science, Bauhaus-Universität Weimar, Weimar, Thüringen, Germany

<sup>3</sup> Slovenian National Building and Civil Engineering Institute, Ljubljana, Slovenia

<sup>4</sup> Department of Materials, Mechanics, Management & Design, Faculty of Civil Engineering and Geoscience, Delft University of Technology, Delft, The Netherlands

other challenges such as hygroscopicity or carbonation leading to decreased shelf-life [15]. The dry-form activator can be ground with precursor, or both can be ground individually and then mixed.

Given the volume of publications on AAMs, it is astonishing that only few papers examine systematically the differences between one-part and two-part AAMs using identical mix designs in both systems and their durability properties. Wang et al. [16] obtained higher compressive strength for alkali-activated blast furnace slag (GGBFS) mortar when using sodium silicate solution (120 MPa) in comparison to powder-form sodium silicate (10–80 MPa). They also noted that strength development with solid activator is more sensitive to the physical and chemical changes (such as water absorption by the solid sodium silicate) [16]. Another example is the work of Collins and Sanjayan [17] in which they compared the use of solid and dissolved sodium silicate to prepare alkali-activated GGBFS concrete: the dry-form activator resulted in better workability and the authors explained this by the slower release of alkali ions in contrast to the solution-form activator.

The present work aims to compare AAMs, containing mineral wools and GGBFS as precursors, prepared via one-part and two-part pathways. Mineral wools have been much less studied as AAM precursors compared to GGBFS, but results show that they have promising reactivity as cementitious material [18–24]. Mineral wool was selected as a co-precursor to supplement the use of blast furnace slag and as a pathway to recycle the waste produced during industrial production, and construction and demolition process in cementitious application. Currently, the mineral waste is underutilized and with an annual production of 2.5 million tons in Europe alone [25], finding pathways to utilize them in high-value products is attractive. The amount of this waste produced annually is projected to increase globally due to emerging energy efficiency which will increase the demand for mineral wool [22]. There are two main types of mineral wools: stone wool and glass wool. Stone wool depicts composition similar to GGBFS, but with variable CaO, MgO, and Al<sub>2</sub>O<sub>3</sub> contents, while glass wool composition is nearly identical to ordinary soda-lime glass [26]. Varying CaO, MgO, and Al<sub>2</sub>O<sub>3</sub> contents have been shown to influence the precursor reactivity and formation of cementitious phases [27–30]. Thus, a binder consisting of GGBFS, stone wool, and glass wool provides information not just for this mix,

but for mixes using GGBFS's that have unusual chemical composition and soda-lime glasses also.

One-part and two-part systems were prepared so that their composition in terms of molar oxide ratios is the same. This study aims to fill the above-mentioned knowledge gap related to the systematic comparison of one- and two-part AAMs and their durability. The gained information has both fundamental and applied implications for the development of new dry-mix formulations as well as understanding the behavior of reported mix designs in the literature. The prepared AAMs were analyzed for reaction kinetics by isothermal calorimetry, fresh and hardened properties (spread value, setting time, compressive strength, abrasion resistance, length change), composition and microstructure, as well as comprehensive durability characterization (sulfate resistance, chloride penetration, carbonation depth, abrasion, and freeze–thaw resistance).

## Materials and methods

### Materials

The GGBFS ( $d_{50} = 10.8 \mu\text{m}$ ) used in this investigation was obtained from Finnsementti (Finland), resin-free glass wool (GW) and stone wool (SW) further referred to as mineral wool were used as co-binder with the slag. The mineral wools were ground in a ball mill in a similar procedure described in [19]. The chemical compositions as analyzed through X-ray fluorescence (PANalytical Omnia Axios-max) are represented in Table 1. Glass wool contains also ~4 w.% of B<sub>2</sub>O<sub>3</sub> [26], which is not detectable with the XRF method used here. Anhydrous sodium metasilicate (modulus of SiO<sub>2</sub>/Na<sub>2</sub>O = 0.9; Alfa Aesar), sodium silicate solution (55.1 wt.% of H<sub>2</sub>O, SiO<sub>2</sub>/Na<sub>2</sub>O modulus of 2.12) and sodium hydroxide pellets (>99% pure; Sigma-Aldrich) were used as alkali activators. Sodium metasilicate was further ground using mortar grinder (RM 200, Retsch) for 10 min. For the two-part analysis, sodium hydroxide and sodium silicate solution were mixed a day before the experiment to ensure mixture equilibration.

Standard sand conforming with EN 196-1 was used as aggregates in the mortars and deionized water was used as added water. The particle size distribution of the materials was analyzed through the laser diffraction technique

**Table 1** Chemical composition of the precursors

Oxides (%)	CaO	Al <sub>2</sub> O <sub>3</sub>	SiO <sub>2</sub>	MgO	Fe <sub>2</sub> O <sub>3</sub>	Na <sub>2</sub> O	K <sub>2</sub> O	SO <sub>3</sub>	LOI <sup>a</sup> 950 °C
BFS	38.5	9.5	32.3	10.2	1.23	0.5	0.5	4.0	–1.3
SW	17.9	16.3	40.4	11.2	8.8	1.4	0.6	0.1	2.5
GW	8.2	1.5	63.3	3.1	0.5	16.5	0.5	0.2	0.0

<sup>a</sup>Loss on ignition

(Beckman Coulter 13320) using the Fraunhofer model. Iso-propanol was used as the dispersion medium to avert the reaction of particles during the measurement.

### Sample preparation

For one-part mortars, the dry materials (GGBFS, anhydrous activator, and mineral wools) were homogenized by mixing them in Kenwood mixer for 1 min before they were mixed in deionized water. To achieve good workability, the dry materials were added to water and not water to dry materials. The slurry was then mixed for 2 min, and standard sand was added and mixed further for another 1 min for a total of 4 min mixing time. Similarly, for the two-part mortars, the GGBFS and mineral wools were homogenized before activating solution was added and mixed using the same parameters (see Table 2). The water-to-binder (w/b) and sand-to-binder (s/b) ratio were both kept constant at 0.40 and 3, respectively.

The mortars were cast in a sealed rectangular  $40 \times 40 \times 160 \text{ mm}^3$  mold and jolted on a vibrating table, then cured at room temperature and demolded after 24 h. The demolded samples were kept in sealed bags at room temperature until testing time. For drying shrinkage, the samples were cured at a controlled condition ( $50\% \pm 5$  relative humidity and  $22 \pm 2 \text{ }^\circ\text{C}$ ) after demolding.

For paste samples used in analytical tests, the mixing was done using high shear mixer (RZR 2020, Heidolph) at 1250 rpm for approximately 5-min mixing time.

### Fresh and hardened properties of specimens

To determine the mechanical properties of the mortars, compressive strength was measured after 1-, 7-, 28- and 90-day age of the mortars, using testing instrument (Z100, Zwick/Roell) with a maximum loading force of 100 kN and force speed used was 2.4 kN/s. Setting time of the paste mix was determined using an automatic Vicat apparatus (Vicatron Matec) according to standard EN 196-3 [31]. The flowability of both mixtures was ascertained using the flow table method specified in SFS-EN 1015-3 [32]. In the flow table method, the mortar slurry is compacted into a conical mold using a tamper. The mold is then removed gently, and the flow table is jolted 15 times to spread the mortar. Finally, the diameter of the spread is measured.

**Table 2** Mix composition (as weight-%) for the dry-mix (DM) and wet-mix (WM) mortar samples

Mix	BFS (%)	SW (%)	GW (%)	Activator (%) <sup>a</sup>	Na/Si (mol) <sup>b</sup>	w/b	s/b
DM (one-part)	22	17	49	12	1.06	0.40	3
WM (two-part)	22	17	49	12	1.06	0.40	3

<sup>a</sup>Activator's solid content in wt-%

<sup>b</sup>Modulus of activating sodium silicate (anhydrous & solution)

### Paste sample characterization

The paste samples used for characterization analyses were stopped at 7, 28, and 90 days through the solvent exchange technique, using isopropanol as described in previous literature [33, 34]. The reaction kinetics was measured using an isothermal microcalorimeter (TAM air, TA Instruments) at  $23 \text{ }^\circ\text{C}$ . The heat flow of reaction was normalized using the weight of solid materials in each paste samples. Thermogravimetric analysis (TGA) was done using Precisa Gravimetrics AG. The samples weighted between 0.5 and 1.5 g, were heated from 24 to  $1100 \text{ }^\circ\text{C}$  at  $10 \text{ }^\circ\text{C}/\text{min}$  in an inert nitrogen atmosphere.

The microstructure of the paste samples was analyzed using scanning electron microscopy (SEM). The 90-day-old paste samples were impregnated with epoxy resin under vacuum, and then polished using diamond pastes. To achieve electric conductivity, the polished section was then coated with 8–10 nm carbon. The backscattered electron (BSE) imaging and an energy-dispersive X-ray spectroscopy (EDX) analysis were carried out at a 12 kV acceleration voltage and 1.6nA electron current using a high-resolution field emission SEM (Helios G4UX, ThermoScientific, equipped with an XMax80 EDX detector, Oxford Instruments).

### Durability properties of hardened mortars

#### Sulfate attack

To examine the mortars resistance to chemical attack, sulfate attack test was undertaken on the mortars after 90 days. Duplicate mortar samples ( $40 \times 40 \times 160 \text{ mm}^3$ ) of each mix were fully immersed in a solution made of 5% sodium sulfate and 3% sodium chloride. Visual observation and mechanical test were used to examine the mortars after 90-day immersion in the solution.

#### Chloride migration

The chloride migration property was evaluated according to the rapid chloride migration (RCM) test described in NT Build 492 [35]. The samples were cylinder slices with a thickness of 50 mm and a diameter of 100 mm. After curing for 28 days, the samples were saturated in a vacuum chamber. The air pressure was reduced till 3 kPa in a few minutes

and the vacuum was maintained for 3 h, followed by filling the container with saturated  $\text{Ca}(\text{OH})_2$  solution until the samples were immersed. The vacuum was kept for 1 h before the container was taken out and the specimens were kept in the solution for another 18 h in ambient condition before subjected to RCM test. 10 wt.% NaCl solution and 0.3 M NaOH solution were used as the catholyte and anolyte, respectively, in the RCM test. The initial voltage applied on the samples was 30 V and then adjusted to 10 V due to the high initial current, 324 mA and 369 mA for DM and WM, respectively. The new current after the adjustment was 91 mA for dry mix and 119 mA for wet mix. The slightly higher initial current for the wet mix indicates that it has lower resistance than the dry mix, while lower resistance is normally associated with a more porous structure of cementitious materials [36]. The test duration of RCM was 24 h and temperature of the whole room was kept at 22 °C.

After the test, the specimens were axially split, and surfaces exposed were sprayed with silver nitrate solution (0.1 M). The penetration depth of chloride was then measured according to the color change due to precipitation of silver chloride. Based on the depth results, the non-steady-state migration coefficient of the mixture can be calculated from Eq. (1):

$$D_{nssm} = \frac{RT}{FE} \cdot \frac{x_d - \alpha \sqrt{x_d}}{t}, \quad (1)$$

with:

$$E = \frac{U - 2}{l}, \quad (2)$$

$$\alpha = 2 \sqrt{\frac{RT}{FE}} \cdot \text{erf}^{-1} \left( 1 - \frac{2c_d}{c_0} \right), \quad (3)$$

where  $D_{nssm}$  is the non-steady-state migration coefficient,  $\text{m}^2/\text{s}$ ;  $F$  is the Faraday constant,  $9.648 \times 10^4 \text{ J}/(\text{V}\cdot\text{mol})$ ;  $U$  is the absolute value of the applied voltage, V;  $R$  is the gas constant,  $8.314 \text{ J}/(\text{K}\cdot\text{mol})$ ;  $T$  is the average value of the initial and final temperatures in the anolyte solution, K;  $l$  is the thickness of the specimen, m;  $x_d$  is the average value of the penetration depths, m;  $t$  is the test duration, seconds;  $\text{erf}^{-1}$  is the inverse of error function;  $c_d$  is the chloride concentration at which the color changes, 0.07 M for OPC and alkali-activated materials [37];  $c_0$  is the chloride concentration in the catholyte solution, 2 M.

### Carbonation tests

The carbonation resistance of the two mixtures was also measured, partially following NEN-EN 12390-12 [38]. The accelerated carbonation was performed in a  $\text{CO}_2$  chamber where  $\text{CO}_2$  concentration, temperature and relative humidity

were controlled. The  $\text{CO}_2$  concentration was kept at 1% v/v, chosen according to [39] which reported that conducting accelerated carbonation using  $\text{CO}_2$  concentrations beyond 1% v/v will not accurately replicate the carbonation mechanisms observed in practice. The inlet flow of  $\text{CO}_2$  was kept constant at the rate of  $100 \text{ cm}^3/\text{min}$ . The temperature in the chamber has been regulated at 20 °C and a relative humidity at 60%. The carbonation test started after 28 days of curing plus 14 days of preconditioning (drying at relative humidity of 55%). The exposure periods in  $\text{CO}_2$  were 7, 28 and 70 days in the test chamber. The carbonation depth was measured with phenolphthalein, according to the standard EN 13295 [40]. The prisms ( $40 \times 40 \times 160 \text{ mm}^3$ ) were split and the fresh surface was sprayed with a 1 wt.% phenolphthalein solution (comprising 1 g of phenolphthalein in a solution of 70 mL ethanol and 30 ml deionized water). The recorded carbonation depths are the average of measurements at 10 locations on the sample and 2 replicated samples were tested for each mixture.

According to the carbonation depths in various curing ages, the carbonation rate can be calculated according to Eq. 4.

$$d_k = a + K_{AC} \sqrt{t}, \quad (4)$$

where  $d_k$  is the mean carbonation depth at time  $t$ , mm;  $a$  is the intercept, mm;  $K_{AC}$  is the carbonation rate,  $\text{mm}/\text{days}^{1/2}$ ;  $t$  is exposure time, days.

### Abrasion test

The abrasion test was performed following EN 1338–annex G [41] by abrading the upper face of testing block of  $100 \times 100 \times 15 \text{ mm}^3$  size with an abrasive material under standard condition. For abrasion resistance the wearing machine Gabbrielli and vernier caliper were used. The flow of the abrasive material was 2.5 l / 75 revolutions.

### Length change

The length change due to drying and/or autogenous shrinkage measurements were carried out on triplicate prism samples with dimensions of  $40 \times 40 \times 160 \text{ mm}^3$  stored and cured after demolding at room temperature and relative humidity of 60%, according to ASTM C596 [42]. The length measurement was carried out using a Matest E077 kit length comparator at the age of 1, 3, 7, 14, 28, and 60 days after casting. The length change ( $LC$ ) over time was then calculated using Eq. (5).

$$\Delta L(\%) = \frac{L_i - L_x}{G} \times 100, \quad (5)$$

where  $L_i$  is the difference between the comparator reading and the reference bar at 1 day,  $L_x$  is the length at each measurement day and  $G$  is the nominal effective length.

### Freeze–thaw test methods

To verify the durability of alkali-activated mortars under cold weather conditions, the freeze–thaw test was performed. Samples with dimension of  $100 \times 100 \times 15$  mm were immersed in water at room temperatures for 24 h after sample age of 28 days. Then they were exposed to 150 freeze–thaw cycles, with temperature operating range from  $(-15 \pm 2)$  °C to  $(+15 \pm 2)$  °C and a humidity range from 10% to 95% in accordance with standard procedure [43]. Each cycle involves lowering of the temperature of the samples from  $+15$  °C to  $-15$  °C in 2 h and another 2 h to maintain the temperature at  $-15$  °C, then the temperature is increased from  $-15$  °C to  $+15$  °C for 2 h and allowed to thaw for another 2 h at  $15$  °C. After 150 cycles, samples were evaluated by visual observations relating to a change in characteristics of the surface and any distortion at the edges of the samples shall also be reported. The results for the drying shrinkage and freeze–thaw are documented in the supplementary files (Figs. S1 and S2).

## Results and discussion

### Reaction kinetics and setting time

The one-part synthesis usually results in rapid-setting of the paste, similar trend was observed here (Table 3). The DM achieved initial setting time after 98 min; while for WM, the initial setting time was twice longer. Though initial setting time specification is arbitrary depending on the application and strength value, the value achieved here for DM can be considered suitable. Conferring to BS EN 197-1 standard specifications [44], the minimum initial setting time required for a cement with compressive strength value of 32.5 MPa (at 28 days) is 75 min. The flowability of the mortar slurry showed WM with a higher spread at 256 mm than DM. This is partly attributed to the water absorption by the anhydrous sodium silicate during mixing affecting the rheology of the DM mix.

The heat evolved (normalized to solid mass of the paste) during 250 h of reaction shows the similarity in the reaction kinetics of the two samples (Fig. 1). It should be noted that heat flow data for 45 min after inserting into the isothermal calorimetry was not used due to the waiting period for the

equilibration of the microcalorimetry after mixing ex situ. Hence, the heat released due to wetting and partial dissolution of the precursors during this period is not fully represented in Fig. 2. There was a very short induction period, as the polymerization and condensation of the dissolved ionic species formed an exothermic peak between 5 and 25 h. This peak is similar to most alkali-activated binders calorimetric peaks and is known as the acceleration and deceleration period [45]. During this period, WM exhibited higher heat released than DM, which is not consistent with the strength development during the first 24 h. Normally, higher heat released can be assumed to be proportional to increased formation of reaction products and consequently strength gain. Nevertheless,

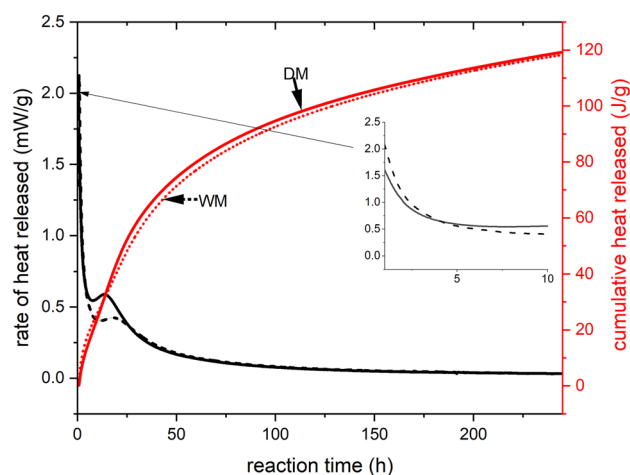


**Fig. 1** Heat evolution curves for DM and AM pastes during 250 h of reaction (inset: shows the initial peak in the first 10 h)

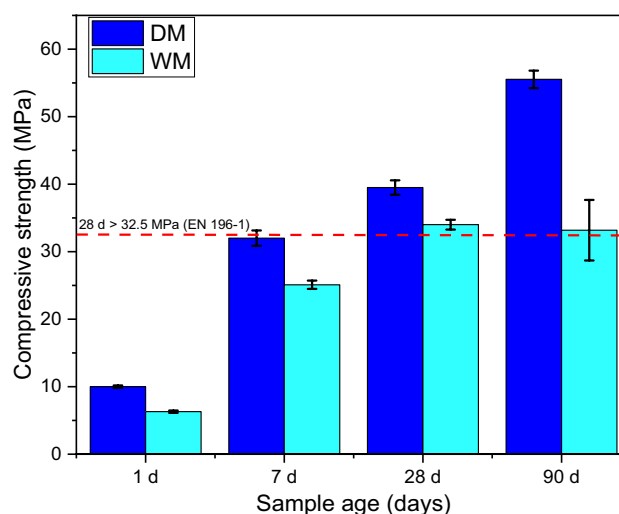


**Fig. 2** Compressive strength of the mortars (DM and WM) at 1–90 days

**Table 3** Setting time and flowability measurements for both samples

Sample	Initial (min)	Final (min)	Spread (mm)
DM	98	166	243
WM	185	280	256

the cumulative heat flow curves showed DM to have a slightly higher total heat released than WM after 250 h.

### Effect on strength development

The compressive strength of the mortars (Fig. 2) increases by time, with DM exhibiting the highest strength of 56 MPa recorded at 90 days. After 1 day, DM had 10 MPa compared to 7 MPa for WM which shows the significance of the one-part (sodium metasilicate) mechanism for early-age strength mortars specifications. The higher early-age strength of DM can be attributed to the higher reaction degree as seen in the calorimetry analysis when sodium metasilicate powder comes in contact with water: the heat released increases the dissolution rate of the precursors and hardening of cementitious phases. This extensive heat release was not, however, detrimental on the flowability of the mix. This is consistent with previous observations on rapid hardening of one-part geopolymers [46, 47].

### Characterization of reaction products using SEM and TGA.

The SEM-BSE images and EDX phase maps constructed from elemental distribution maps of the binders after 90 days of curing are shown in Fig. 3. The EDX phase maps enable the identification of reacted and unreacted phases and their spatial distribution. Reacted (cyan) and unreacted areas (black) of the binder microstructure are exemplary shown in the Fig. 3. Both mixes show similar phase distributions and microstructure, the quantification of reacted matrix composition is shown in Table 4. Results clearly show that only minor deviation in composition is observed. In addition, the phase maps (see Fig. S3) show reaction rims around unreacted GGBFS grains consistent with Mg–Al layered double hydroxide (LDH) formation, these rims are a little more significant in DM than for WM. But a larger area giving statistical evidence needs to be analyzed to verify this observation. The Mg–Al LDH formation is in line with expectations of reaction products formed in alkali-activated GGBFS-based binders with high MgO content [27, 48]. The elemental distributions of this matrix are further shown in Fig. S3.

Figure 4 illustrates the differential thermogravimetry (DTG) curve for the paste samples of both DM and WM

**Fig. 3** SEM-BSE images and phase maps of (a) DM and (b) WM at 90 days of reaction (cyan—reaction products and black—unreacted particles)

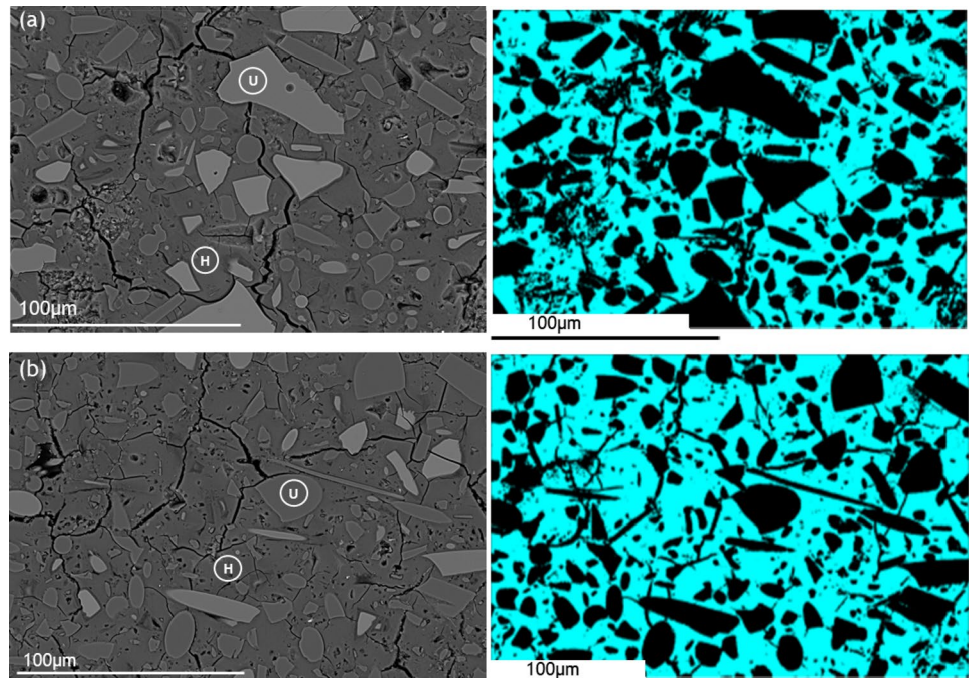


**Table 4** Elemental composition of the reaction products (given in oxide wt.-%)

Spectrum Label	Na <sub>2</sub> O	MgO	Al <sub>2</sub> O <sub>3</sub>	SiO <sub>2</sub>	SO <sub>3</sub>	K <sub>2</sub> O	CaO	TiO <sub>2</sub>	MnO	Fe <sub>2</sub> O <sub>3</sub>	Total
DM	9.3	5.4	5.0	52.9	0.95	0.6	24.3	0.5	0.3	0.7	100.00
WM	10.0	5.6	5.4	54.6	0.5	0.8	21.4	0.6	0.2	1.0	100.00

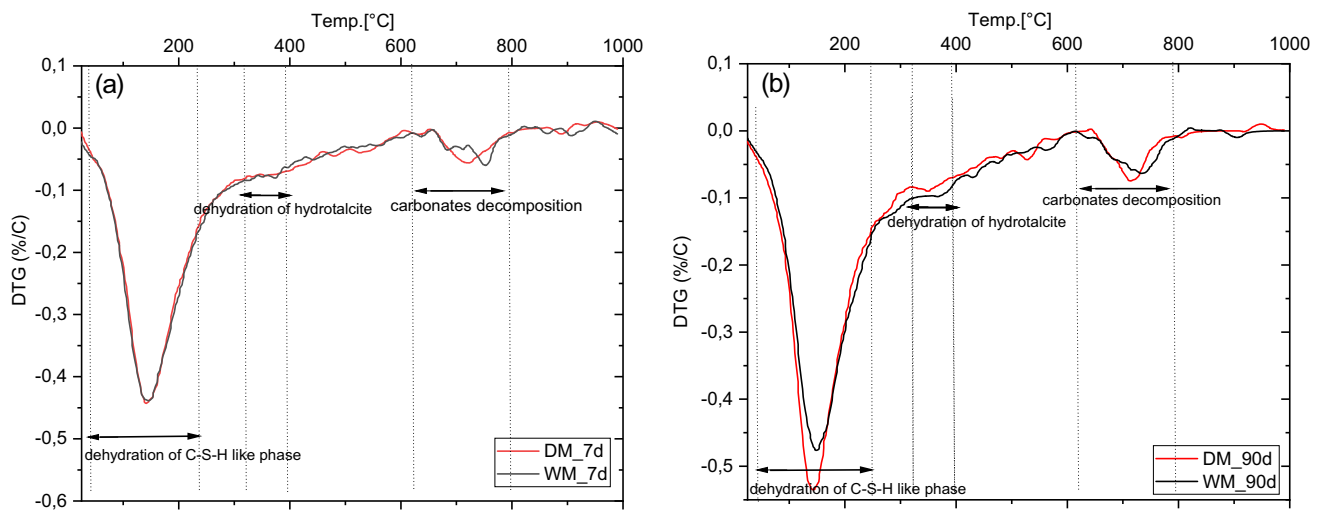


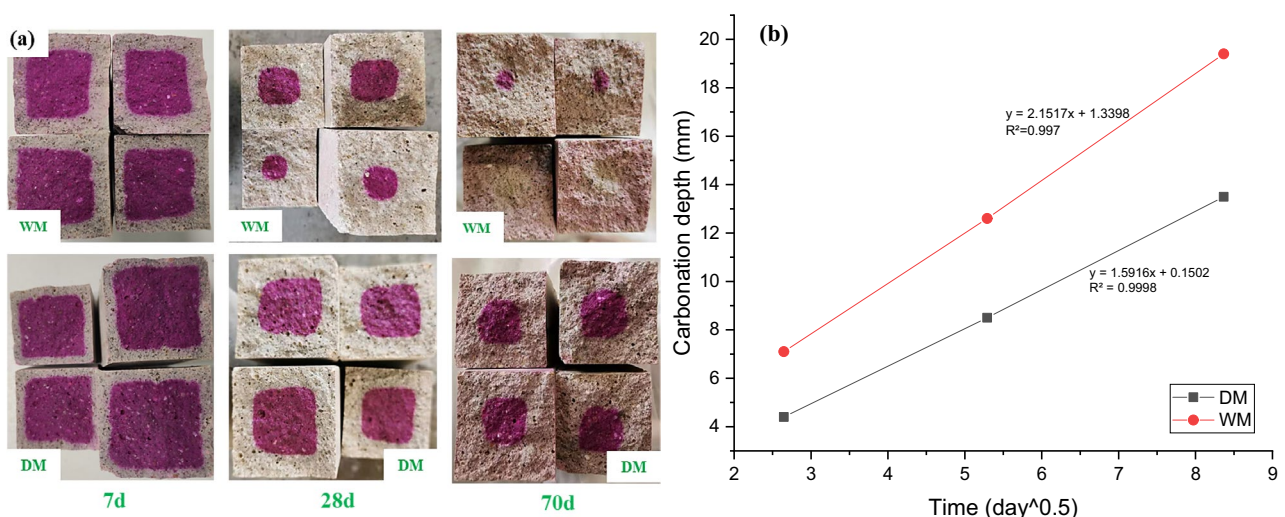
**Fig. 4** DTG curves for (a) 7-day pastes and (b) at 28 days showing the decomposition peaks for suggested reaction products

at early and later ages. Both binders displayed similar DTG curves true to form, as the difference between the samples is only the synthesis pathway used. Regardless of the pathway, the reaction products observed according to decomposition temperature peaks were; (i) the peak between 90 °C and 210 °C are due to dehydration of free water and degradation of C-(A)-S-H type phases in the binder [49, 50]. Although not calculated, the intensity of the peak may suggest higher amount of reaction product available and degraded; (ii) the presence of Mg–Al LDH phase (i.e., hydrotalcite) is seen in the 300–350 °C region consistent with the observations in SEM; and (iii) decarbonation peaks at 650–700 °C [50]. The dehydration of the C-(A)-S-H and hydrotalcite phases were more intense at 28 days than at 7 days.

## Durability

### Carbonation

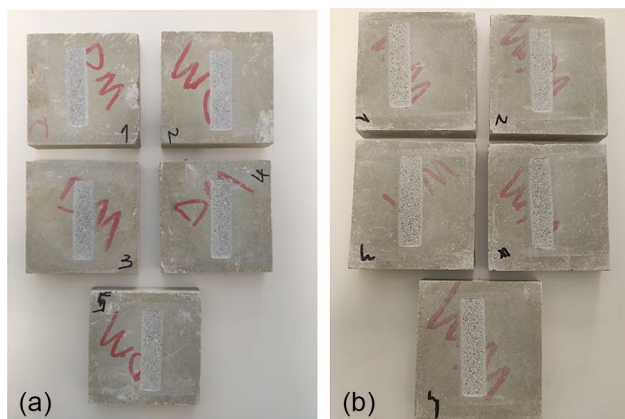
According to the carbonation depths at various ages calculated using Eq. 4, the carbonation rates of the two mixtures were calculated to be 1.59 and 2.15 mm/days<sup>1/2</sup>, respectively, as shown in Fig. 5. The larger carbonation rate of wet mix indicates that it is less resistant to carbonation and more porous when compared to the dry mix mortar, and thus less durable under ingress of external chemicals. This information is consistent with the RCM results discussed in the following section.



**Fig. 5** (a) Cross-sectional images of carbonated DM and WM, and (b) carbonation rates of dry and wet mix as a function of time

**Table 5** Chloride penetration depth and migration coefficient

Mixture	$X_d$ (mm)	Migration coefficient ( $m^2/s$ )
DM	$5.6 \pm 1.1$	$5.8 \times 10^{-12}$
WM	$7.6 \pm 1.3$	$8.7 \times 10^{-12}$

**Fig. 6** Images of the abrasion paths for (a) DM and (b) WM

### Rapid chloride migration

The penetration depth and migration coefficient of the mixtures are shown in Table 5. The reported results are averages of 3 specimens. The migration coefficients of the two mixtures fall in a similar range of that reported for AAM-based system [37]. The higher migration coefficient of WM compared to DM indicates that the former is less resistant to chloride penetration.

Binder porosity and pore solution chemistry have been previously reported to impact on the rate of chloride permeability [37, 51], which may suggest higher porosity in WM than in DM.

### Abrasion

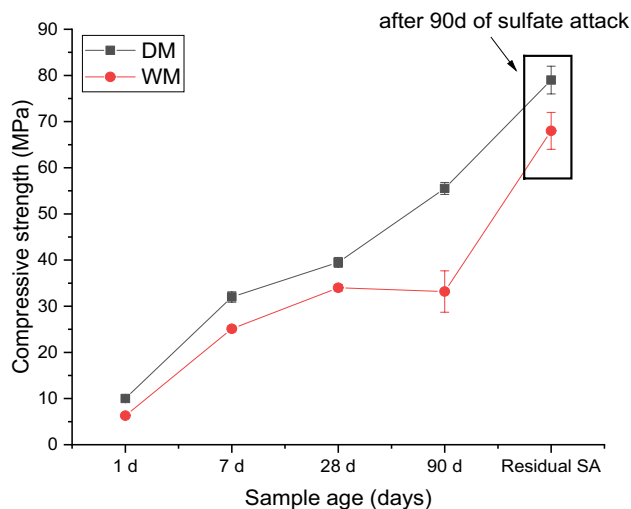
Mortars or concretes used in flooring or as pavement are subjected to wear caused by abrasion. The abrasion resistance is the ability of these material surfaces to withstand the wear, rubbing and scrapping. Figure 6 shows the abraded mortars after several revolutions. According to the results in Table 6, both DM and WM exhibited high and similar abrasion resistance when compared to OPC.

### Sulfate attack

Under the investigated experimental conditions, both mortars exhibited high resistance to aggressive conditions. The

**Table 6** Measurements and classification of the mortars

Sample	Testing location	Average length of the groove [mm]	EN 1338 classification
DM	Middle of the sample	19.0	Class I
WM		18.9	
OPC		22.1	Class H

**Fig. 7** Residual strength after 90 days of sulfate attack on the mortars

compressive strength of both mortars analyzed after 90 days in sulfate and chloride solution increased significantly (Fig. 7). The WM strength after exposure doubled when compared with the 90-day reference of non-exposed mortars, while DM increased by approximately 75%. This shows continuous formation of reaction products during the test and no deterioration on the reaction products while under aggressive conditions. Similar strength improvement after sulfate attack (SA) have been reported for AAM binders [52, 53]. AAM binders are known to have low permeability properties compared to OPC, this property helps in mitigating the penetration of aggressive ions into the mortar [53, 54]. Overall, the durability of these mortars showed considerable resistivity to severe environmental attacks (also see Fig. S2).

### Conclusion

The pathway in which alkali activator is introduced during alkali activation of GGBFS and mineral wool influences the synthesis of the reaction products and their physical properties. One-part (DM) and two-part (WM) alkali activation pathways were explored and compared. Here, this study aimed to utilize mineral wools residues in alkali-activated



materials in one-part and two-part synthesis for comparisons. The experimental investigation shows that one-part synthesis in the alkali activation of GGBFS and mineral wool exhibited good mechanical properties presented by the one-part synthesis, while the durability tests show that the DM exhibits good resistance to the sulfate attack, and a lower carbonation depth in comparison to the WM synthesis.

The activator state has a significant effect on the fresh and hardened properties. The DM exhibited short setting time at 98 min and flowability spread of 243 mm compared to 185 min and 256 mm, respectively, for WM. Reaction products detected using DTG were phases consistent to C–A–S–H consistent with alkali-activated slags and the presence of Mg–Al LDH phase likely hydrotalcite. Compressive strength achieved for DM after 28 days was 38 MPa and 34 MPa for WM. However, DM experienced a significant increment in strength of 56 MPa at 90 days compared to 34 MPa for WM.

Both mortars showed considerable resistivity to sulfate attack and freeze–thaw as their physical and mechanical properties improved during exposure to these severe conditions. In fact, the residual compressive strength for WM after sulfate attack doubled compared to its strength at 28 days. Under abrasive conditions important for industrial flooring, both mortars exhibited good resistance to abrasive wear with an EN 1338 I classification better than conventional cement mortars. In conclusion, the study shows the potential of the one-part synthesis in the utilization of industrial residues (i.e., mineral wools) in cementitious application.

**Supplementary Information** The online version contains supplementary material available at <https://doi.org/10.1007/s10163-023-01878-3>.

**Acknowledgements** This research was undertaken in the framework of WOOL2LOOP H2020 project with grant number #821000. Elijah Adesanya acknowledges the Finnish Cultural Foundation for the post-doctoral research grant (grant #00201230). Juho Yliniemi and Tero Luukkonen wish to acknowledge funding from the Academy of Finland (grants #322786 and #326291, respectively). Jarno Karvonen, Elisa Wirkkala and Jani Österlund are acknowledged for their contributions to the laboratory work.

**Funding** Open Access funding provided by University of Oulu (including Oulu University Hospital).

## Declarations

**Conflict of interest** The authors declare that they have no known competing financial interests or personal relationships that could have appeared to influence the work reported in this paper.

**Open Access** This article is licensed under a Creative Commons Attribution 4.0 International License, which permits use, sharing, adaptation, distribution and reproduction in any medium or format, as long as you give appropriate credit to the original author(s) and the source, provide a link to the Creative Commons licence, and indicate if changes were made. The images or other third party material in this article are included in the article's Creative Commons licence, unless indicated

otherwise in a credit line to the material. If material is not included in the article's Creative Commons licence and your intended use is not permitted by statutory regulation or exceeds the permitted use, you will need to obtain permission directly from the copyright holder. To view a copy of this licence, visit <http://creativecommons.org/licenses/by/4.0/>.

## References

1. Provis J (2014) Alkali activated materials, 1st edn. Springer Netherlands. [https://www.rilem.net/docs/2014090109\\_star-224-aam\\_final-draft\\_full.pdf](https://www.rilem.net/docs/2014090109_star-224-aam_final-draft_full.pdf)
2. Lecomte I, Henrist C, Liégeois M, Maseri F, Rulmont A, Cloots R (2006) (Micro)-structural comparison between geopolymers, alkali-activated slag cement and Portland cement. *J Eur Ceram Soc* 26:3789–3797. <https://doi.org/10.1016/j.jeurceramsoc.2005.12.021>
3. Jackson MD, Mulcahy SR, Chen H, Li Y, Li Q, Cappelletti P, Wenk H-R (2017) Phillipsite and Al-tobermorite mineral cements produced through low-temperature water-rock reactions in Roman marine concrete. *Am Miner* 102:1435–1450. <https://doi.org/10.2138/am-2017-5993CCBY>
4. Seymour LM, Tamura N, Jackson MD, Masic A (2022) Reactive binder and aggregate interfacial zones in the mortar of Tomb of Caecilia Metella concrete, 1C BCE, Rome. *J Am Ceram Soc* 105:1503–1518. <https://doi.org/10.1111/jace.18133>
5. Adesanya E, Perumal P, Luukkonen T, Yliniemi J, Ohenoja K, Kinnunen P, Illikainen M (2021) Opportunities to improve sustainability of alkali-activated materials: a review of side-stream based activators. *J Clean Prod* 286:125558. <https://doi.org/10.1016/j.jclepro.2020.125558>
6. Shobeiri V, Bennett B, Xie T, Visintin P (2021) A comprehensive assessment of the global warming potential of geopolymer concrete. *J Clean Prod* 297:126669. <https://doi.org/10.1016/j.jclepro.2021.126669>
7. Palomo A, Maltseva O, Garcia-Lodeiro I, Fernández-Jiménez A (2021) Portland versus alkaline cement: continuity or clean break: “a key decision for global sustainability.” *Front Chem*. <https://doi.org/10.3389/fchem.2021.705475>
8. Luukkonen T, Abdollahnejad Z, Yliniemi J, Kinnunen P, Illikainen M (2018) One-part alkali-activated materials: a review. *Cem Concr Res* 103:21–23. <https://doi.org/10.1016/j.cemconres.2017.10.001>
9. Whiting J (1895) Manufacture of cement. Patent US544706 A., US544706 A. <http://www.google.com/patents/US544706>. Accessed 5 July 2016
10. Kuehl H (1908) Slag cement and process of making the same. US900939A. <https://patents.google.com/patent/US900939A/en>. Accessed 1 Nov 2021
11. Adesanya E, Ohenoja K, Luukkonen T, Kinnunen P, Illikainen M (2018) One-part geopolymer cement from slag and pretreated paper sludge. *J Clean Prod*. <https://doi.org/10.1016/j.jclepro.2018.03.007>
12. Chamlers DP, Ktdd PG, Sleep PD (2015) Geopolymer cement
13. Deventer JSJV, Feng D, Duxson P (2010) Dry mix cement composition, methods and systems involving same. US7691198B2. <https://patents.google.com/patent/US7691198B2/en>. Accessed 1 Nov 2021
14. Luukkonen T, Yliniemi J, Abdollahnejad Z (2022) 4 – Alkali-activated dry-mix concretes. In: Pacheco-Torgal F, Chindaprasirt P, Ozbakkaloglu T (eds) Handbook of advances in alkali-activated concrete. Woodhead Publishing, pp 67–88. <https://doi.org/10.1016/B978-0-323-85469-6.00008-8>

15. Matalkah F, Soroushian P (2019) Shelf life of alkali activated cement: Effects of storage condition and duration. *Constr Build Mater* 222:664–672. <https://doi.org/10.1016/j.conbuildmat.2019.06.193>
16. Wang S-D, Scrivener KL, Pratt PL (1994) Factors affecting the strength of alkali-activated slag. *Cem Concr Res* 24:1033–1043. [https://doi.org/10.1016/0008-8846\(94\)90026-4](https://doi.org/10.1016/0008-8846(94)90026-4)
17. Collins FG, Sanjayan JG (1999) Workability and mechanical properties of alkali activated slag concrete. *Cem Concr Res* 29:455–458. [https://doi.org/10.1016/S0008-8846\(98\)00236-1](https://doi.org/10.1016/S0008-8846(98)00236-1)
18. Kinnunen P, Yliniemi J, Talling B, Illikainen M (2017) Rock-wool waste in fly ash geopolymer composites. *J Mater Cycles Waste Manage* 19:1220–1227. <https://doi.org/10.1007/s10163-016-0514-z>
19. Yliniemi J, Walkley B, Provis JL, Kinnunen P, Illikainen M (2020) Nanostructural evolution of alkali-activated mineral wools. *Cem Concr Compos* 106:103472. <https://doi.org/10.1016/j.cemconcomp.2019.103472>
20. Alzaza A, Mastali M, Kinnunen P, Korat L, Abdollahnejad Z, Ducman V, Illikainen M (2019) Production of lightweight alkali activated mortars using mineral wools. *Materials (Basel)* 12:1695. <https://doi.org/10.3390/ma12101695>
21. Pavlin M, Horvat B, Frankovič A, Ducman V (2021) Mechanical, microstructural and mineralogical evaluation of alkali-activated waste glass and stone wool. *Ceram Int*. <https://doi.org/10.1016/j.ceramint.2021.02.068>
22. Yliniemi J, Walkley B, Provis JL, Kinnunen P, Illikainen M (2020) Influence of activator type on reaction kinetics, setting time, and compressive strength of alkali-activated mineral wools. *J Therm Anal Calorim*. <https://doi.org/10.1007/s10973-020-09651-6>
23. Lemougna PN, Adediran A, Yliniemi J, Luukkonen T, Illikainen M (2021) Effect of organic resin in glass wool waste and curing temperature on the synthesis and properties of alkali-activated pastes. *Mater Des* 212:110287. <https://doi.org/10.1016/j.matdes.2021.110287>
24. Adesanya E (2015) Fibre-reinforced mineral wool geopolymer composites
25. Väntsi O, Kärki T (2013) Mineral wool waste in Europe: a review of mineral wool waste quantity, quality, and current recycling methods. *J Mater Cycles Waste Manag* 16:62–72. <https://doi.org/10.1007/s10163-013-0170-5>
26. Yliniemi J, Ramaswamy R, Luukkonen T, Laitinen O, de Sousa AN, Huuhtanen M, Illikainen M (2021) Characterization of mineral wool waste chemical composition, organic resin content and fiber dimensions: aspects for valorization. *Waste Manage* 131:323–330. <https://doi.org/10.1016/j.wasman.2021.06.022>
27. Ben Haha M, Lothenbach B, Le Saout G, Winnefeld F (2012) Influence of slag chemistry on the hydration of alkali-activated blast-furnace slag – Part II: Effect of Al<sub>2</sub>O<sub>3</sub>. *Cem Concr Res* 42:74–83. <https://doi.org/10.1016/j.cemconres.2011.08.005>
28. Ben Haha M, Lothenbach B, Le Saout G, Winnefeld F (2011) Influence of slag chemistry on the hydration of alkali-activated blast-furnace slag – Part I: Effect of MgO. *Cem Concr Res* 41:955–963. <https://doi.org/10.1016/j.cemconres.2011.05.002>
29. Ben Haha M, Le Saout G, Winnefeld F, Lothenbach B (2011) Influence of activator type on hydration kinetics, hydrate assemblage and microstructural development of alkali activated blast-furnace slags. *Cem Concr Res* 41:301–310. <https://doi.org/10.1016/j.cemconres.2010.11.016>
30. Walkley B, San Nicolas R, Sani M-A, Bernal SA, van Deventer JSJ, Provis JL (2017) Structural evolution of synthetic alkali-activated CaO-MgO-Na<sub>2</sub>O-Al<sub>2</sub>O<sub>3</sub>-SiO<sub>2</sub> materials is influenced by Mg content. *Cem Concr Res* 99:155–171. <https://doi.org/10.1016/j.cemconres.2017.05.006>
31. EN 196–3 (n.d.) EN 196–3, Methods of testing cement. Part 3: Determination of setting times and soundness. Finnish Standardization Association. <https://online.sfs.fi/fi/index/tuotteet/SFS/CEN/ID2/1/449135.html.stx>. Accessed 2 Nov 2021
32. EN 1015–3 (1999) Methods of test for mortar for masonry. Determination of consistence of fresh mortar (by flow table). European Committee for Standardization
33. Chavda MA, Bernal SA, Apperley DC, Kinoshita H, Provis JL (2015) Identification of the hydrate gel phases present in phosphate-modified calcium aluminate binders. *Cem Concr Res* 70:21–28. <https://doi.org/10.1016/j.cemconres.2015.01.007>
34. Adesanya E, Sreenivasan H, Kantola AM, Telkki V-V, Ohenoja K, Kinnunen P, Illikainen M (2018) Ladle slag cement–characterization of hydration and conversion. *Constr Build Mater* 193:128–134
35. NORDTEST (1999) Concrete, mortar and cement-based repair materials: chloride migration coefficient from non-steady-state migration experiments (NT BUILD 492), NORDTEST. <http://www.nordtest.info/wp/1999/11/21/concrete-mortar-and-cement-based-repair-materials-chloride-migration-coefficient-from-non-steady-state-migration-experiments-nt-build-492/>. Accessed 10 Dec 2021
36. Chi L, Li W, Li Z, Wang Z, Lu S, Liu Q (2022) Investigation of the hydration properties of cement with EDTA by alternative current impedance spectroscopy. *Cem Concr Compos* 126:104365. <https://doi.org/10.1016/j.cemconcomp.2021.104365>
37. Ravikumar D, Neithalath N (2013) Electrically induced chloride ion transport in alkali activated slag concretes and the influence of microstructure. *Cem Concr Res* 47:31–42. <https://doi.org/10.1016/j.cemconres.2013.01.007>
38. NEN (n.d.) Determination of the carbonation resistance of concrete – accelerated carbonation method. <https://www.nen.nl/en/nen-en-12390-12-2020-en-267754>. Accessed 10 Dec 2021
39. Bernal SA, Provis JL, Walkley B, San Nicolas R, Gehman JD, Brice DG, Kilcullen AR, Duxson P, van Deventer JSJ (2013) Gel nanostructure in alkali-activated binders based on slag and fly ash, and effects of accelerated carbonation. *Cem Concr Res* 53:127–144. <https://doi.org/10.1016/j.cemconres.2013.06.007>
40. SFS (Finnish Standards Association) (n.d.) Products and systems for the protection and repair of concrete structures. Test methods. Determination of resistance to carbonation. <https://online.sfs.fi/fi/index/tuotteet/SFS/CEN/ID2/1/6191.html.stx>. Accessed 10 Dec 2021
41. SFS Online (n.d.) SFS-EN 1338 + AC: en – concrete paving blocks. Requirements and test methods. <https://online.sfs.fi/fi/index/tuotteet/SFS/CEN/ID2/1/6330.html.stx>. Accessed 14 June 2021
42. ASTM-C596 (n.d.) Standard test method for drying shrinkage of mortar containing hydraulic cement. Document Center, Inc. <https://www.document-center.com/standards/show/ASTM-C596>. Accessed 4 Nov 2016
43. ETAG (2013) ETAAG 004 external thermal insulation composite systems with rendering. <https://www.eota.eu/sites/default/files/uploads/ETAGs/etag-004-february-2013.pdf>. Accessed 10 Dec 2021
44. EN 197-1 (2011) EN 197-1 Cement. Part 1: Composition, quality requirements and conformity of common cements. <https://online.sfs.fi/fi/index/tuotteet/SFS/CEN/ID2/1/182891.html.stx>. Accessed 16 Aug 2019
45. Shi C, Day RL (1995) A calorimetric study of early hydration of alkali-slag cements. *Cem Concr Res* 25:1333–1346. [https://doi.org/10.1016/0008-8846\(95\)00126-W](https://doi.org/10.1016/0008-8846(95)00126-W)
46. Adesanya E, Ohenoja K, Di Maria A, Kinnunen P, Illikainen M (2020) Alternative alkali-activator from steel-making waste for one-part alkali-activated slag. *J Clean Prod* 274:123020. <https://doi.org/10.1016/j.jclepro.2020.123020>
47. Suwan T, Fan M (2017) Effect of manufacturing process on the mechanisms and mechanical properties of fly ash-based

- geopolymer in ambient curing temperature. *Mater Manuf Processes* 32:461–467. <https://doi.org/10.1080/10426914.2016.1198013>
48. Ke X, Bernal SA, Provis JL (2016) Controlling the reaction kinetics of sodium carbonate-activated slag cements using calcined layered double hydroxides. *Cem Concr Res* 81:24–37. <https://doi.org/10.1016/j.cemconres.2015.11.012>
  49. Abdel Gawwad HA, Abd El-Aleem S, Ouda AS (2016) Preparation and characterization of one-part non-Portland cement. *Ceram Int* 42:220–228. <https://doi.org/10.1016/j.ceramint.2015.08.096>
  50. Collier NC (2016) Transition and decomposition temperatures of cement phases – a collection of thermal analysis data. *Ceram-Silikaty* 60:338–343. <https://doi.org/10.13168/cs.2016.0050>
  51. Yoon HN, Park SM, Lee HK (2018) Effect of MgO on chloride penetration resistance of alkali-activated binder. *Constr Build Mater* 178:584–592. <https://doi.org/10.1016/j.conbuildmat.2018.05.156>
  52. Džunuzović N, Komljenović M, Nikolić V, Ivanović T (2017) External sulfate attack on alkali-activated fly ash-blast furnace slag composite. *Constr Build Mater* 157:737–747. <https://doi.org/10.1016/j.conbuildmat.2017.09.159>
  53. Komljenović M, Baščarević Z, Marjanović N, Nikolić V (2013) External sulfate attack on alkali-activated slag. *Constr Build Mater* 49:31–39. <https://doi.org/10.1016/j.conbuildmat.2013.08.013>
  54. Shi C (1996) Strength, pore structure and permeability of alkali-activated slag mortars. *Cem Concr Res* 26:1789–1799. [https://doi.org/10.1016/S0008-8846\(96\)00174-3](https://doi.org/10.1016/S0008-8846(96)00174-3)

**Publisher's Note** Springer Nature remains neutral with regard to jurisdictional claims in published maps and institutional affiliations.